

## RESEARCH ARTICLE

10.1002/2017JB014842

## Key Points:

- Cumulative grain-scale changes in stress, strain, and porosity during brittle fracturing match observed bulk behavior
- Discrete element modeling provides a useful technique to quantify and to correlate microstructural changes in stress, strain, and porosity
- Brittle fractures correspond to regions of lower stresses, higher porosity, and highly localized dilation and distortional strain

## Supporting Information:

- Supporting Information S1
- Data Set S1

## Correspondence to:

T. LongJohn,  
tami.longjohn94@gmail.com

## Citation:

LongJohn, T., Morgan, J. K., & Dugan, B. (2018). Microstructural evolution of porosity and stress during the formation of brittle shear fractures: A discrete element model study. *Journal of Geophysical Research: Solid Earth*, 123, 2228–2245. <https://doi.org/10.1002/2017JB014842>

Received 7 AUG 2017

Accepted 23 FEB 2018

Accepted article online 28 FEB 2018

Published online 23 MAR 2018

Corrected 27 APR 2017

The copyright line for this article was changed on 27 APR 2018 after original online publication.

# Microstructural Evolution of Porosity and Stress During the Formation of Brittle Shear Fractures: A Discrete Element Model Study

Tamunoisoala LongJohn<sup>1</sup> , Julia K. Morgan<sup>1</sup> , and Brandon Dugan<sup>1,2</sup> 
<sup>1</sup>Department of Earth Science, Rice University, Houston, TX, USA, <sup>2</sup>Department of Geophysics, Colorado School of Mines, Golden, CO, USA

**Abstract** Brittle fracturing in rocks is a progressive process involving changes in stress, strain, and porosity. Changes in these properties occur heterogeneously within a rock and are manifest at the grain scale, which is difficult to observe directly in the laboratory or the field. This study uses the discrete element method to show that fractures correspond to zones of generally lower stresses, higher porosity, and highly localized dilation and distortional strain. Using the discrete element method, we conducted numerical biaxial experiments at different confining pressures to probe the internal conditions of a low cohesive sandy sediment numerical analog. When compression begins, the stresses within the sandy sediment are relatively homogeneous with anastomosing stress chains. At yield stress, when the confining pressure is relatively low, multiple dilational bands start to open. At peak stress, high-magnitude stress chains localize adjacent to the developing shear band and distortion is evident. Postpeak stress, through-going shear fractures are fully developed. High stresses are transmitted across the fracture where porosity is low through a network of particles in contact. With increasing confining pressure, distortion is favored over dilation during deformation. Also, the number of particles that define the width of a stress chain across a shear fracture, and the steepness of the fracture, increases. Our results can be applied to understanding stress conditions of field samples, and in constraining rock property changes during reservoir modeling of fractured reservoirs.

## 1. Introduction

A mechanistic understanding of brittle fracturing is important in many geoscience and engineering fields (Bieniawski, 1967a; Coates, 1964; Hirata et al., 2007; Hoek & Martin, 2014; Ma & Chen, 2016; Paterson & Wong, 2005). Of particular interest is fracturing relating to drilling and producing wells, and also hazardous waste disposal (Berkowitz, 2002; Boutt & McPherson, 2002), because associated changes in porosity may influence permeability (Bernabé et al., 2003; Friedman, 1976). Porosity and permeability can vary significantly within fractured rock (Fossen et al., 2007; Sulem & Ouffroukh, 2006), as fractures can increase or decrease the total pore volume of a rock (Stearns & Friedman, 1972), which influences storage capacity and fluid transport (Nelson, 2001; Stearns & Friedman, 1972). Thus, a better understanding of the mechanisms of brittle fracturing and related porosity changes contributes to our ability to extract energy and ground water from fractured reservoirs.

Since the 1960s, many laboratory experiments have focused on elucidating the mechanism of brittle fracturing (Bieniawski, 1967a; Brace & Byerlee, 1966; Hallbauer et al., 1973; Handin et al., 1963; Handin & Hager, 1957; Schock et al., 1973). From a macroscopic viewpoint, brittle fracturing is considered to be a discrete event that occurs at a unique peak stress, which is also referred to as failure or fracture stress (Paterson & Wong, 2005). This peak stress can be represented by failure criteria such as the Mohr-Coulomb failure criterion for macroscopic shear fracturing (Jaeger et al., 2007; Paterson & Wong, 2005). Brittle fracturing, however, is a progressive process marked by complicated changes within the material, and simply measuring the peak stress at failure does not fully represent this complexity (Al-Tahini et al., 2006; Hoek & Martin, 2014).

Additionally, stress measurements alone do not provide insights into the mechanisms of brittle fracturing at the grain scale (hereafter, referred to as micromechanisms). Advanced laboratory techniques, such as X-ray computed tomography (CT) and scanning electron microscopy (SEM), have been employed to study microscopic structures and to investigate the micromechanisms of fracturing (Alshibli & Hasan, 2008; Driskill et al., 2013; El Bied et al., 2002; Friedman, 1976; Menendez et al., 1996; Salvatore et al., 2016; Sulem & Ouffroukh, 2006). Nonetheless, there are limitations with laboratory analyses. They can be time-consuming and

expensive, and sample heterogeneity leads to differences in replicate experiments (Schöpfer et al., 2009), necessitating multiple experiments to fully characterize rock behavior. In addition, micromechanisms are difficult to document in real time during laboratory experiments, because the sample is generally hidden from view (Salvatore et al., 2016; Sulem & Ouffroukh, 2006).

Numerical modeling approaches offer the ability to investigate the micromechanisms of brittle fracturing in great detail, and thus complement and expand upon laboratory studies. In particular, discrete numerical methods are attractive because, much like real rocks, numerical materials can be composed of assemblages of grains. Furthermore, in contrast to continuum methods, the mechanical behavior of the model material is not predefined, rather it emerges from particle interactions that evolve as the material evolves (Morgan, 2015; Schöpfer et al., 2009).

The discrete element method (DEM) has been employed to simulate both small-scale laboratory and large-scale geodynamic processes, including the formation of deformation bands in sandstones (Antonellini & Pollard, 1995), the evolution of properties and micromechanics of fault gouges (Guo & Morgan, 2007, 2008), the evolution of slope failure and landslide processes (Katz et al., 2014), and the deformation of contractional wedges and fold and thrust belts (Dean et al., 2013; Morgan, 2015). The effects of particle shape, normal stress, cementation, and stratification have also been examined (Guo & Morgan, 2004; Jiang et al., 2011; Jiang, Liu, et al., 2013; Jiang, Zhang, et al., 2013; Kock & Huhn, 2007a, 2007b). However, only a few of these studies have explored the spatial evolution of fracturing and its relationship to macroscale processes and properties (Jiang, Liu, et al., 2013), and none of these studies provide insights into the spatial distribution of stress and porosity. In this study, we used DEM models to simulate biaxial deformation experiments of numerical analogs to sandy sediments, and we probe these simulations to understand the detailed micromechanical evolution of stress, porosity, and strain during brittle failure.

## 2. Background

The Mohr-Coulomb failure criterion is widely accepted and commonly used to assess macroscopic shear fracturing. The Mohr-Coulomb failure criterion describes the relation of shear stress ( $\tau$ ) and normal stress ( $\sigma_n$ ),

$$\tau = \mu^* \sigma_n + C \quad (1)$$

where  $\mu$  is the coefficient of friction ( $\mu = \tan \phi$ , and  $\phi$  is the angle of internal friction) and  $C$  is cohesion. The Mohr-Coulomb criterion is useful for understanding the limiting conditions for rock stress state at failure (Jaeger et al., 2007). However, it only defines the bulk strength of a rock, whereas many studies have shown that fracturing is a cumulative and progressive process involving grain-scale changes in stress, strain, and porosity (Al-Tahini et al., 2006; Hoek & Martin, 2014). It is the cumulative, grain-scale changes that result in the observed bulk behavior, and variations in these micromechanical processes during deformation are poorly documented.

Bulk changes in stress and volumetric strain, which is related to porosity, have been used to characterize the evolution of brittle fracturing during laboratory experiments (Bieniawski, 1967a, 1967b; Hallbauer et al., 1973; Hoek & Martin, 2014). From these studies, four major stages have been identified during the brittle fracturing process: (I) crack closure, (II) elastic deformation, (III) stable crack growth, and (IV) unstable crack growth (Hoek & Martin, 2014; Paterson & Wong, 2005). Stage I corresponds to a nonlinear elastic increase in bulk stress as preexisting cracks in a rock are closed. Stage II is a linear elastic increase in bulk stress (Hallbauer et al., 1973; Hoek & Martin, 2014). Stage III is the stage of stable crack growth, which begins with crack formation and terminates when more extreme strain localization begins (Hallbauer et al., 1973; Hoek & Martin, 2014). Finally, during stage IV, unstable crack growth results from the coalescence of existing microcracks (Hallbauer et al., 1973; Hoek & Martin, 2014). This localization of strain creates a macroscopic shear band or a fracture (Hallbauer et al., 1973; Hoek & Martin, 2014).

Investigations of changes in rock properties during stages III and IV document the importance of dilatancy (Brace & Byerlee, 1966; Brace et al., 1966; Lambe & Whitman, 1969). Dilatancy refers to the tendency of a rock to undergo inelastic changes in volume (porosity) in response to applied stress (Brace et al., 1966; Paterson & Wong, 2005; Wong et al., 1997). Dilatancy is of practical importance as it may provide premonitory signs for fracturing, and thus has implications for the stability of buildings, dams, tunnels, and mines. Additionally,

dilatancy could be important on a larger scale because it can cause significant changes in volume in a subsurface reservoir.

Because of its significance in rock deformation, dilatancy has been studied extensively in laboratory studies (Brace et al., 1966; Desrues et al., 1985; Jaeger et al., 2007; Paterson & Wong, 2005; Schock et al., 1973; Sulem & Ouffroukh, 2006). Dilatancy typically initiates between 33 and 67% of the peak stress. The magnitude of dilatancy is determined as the maximum departure of the stress-volumetric strain curve from the line representing elastic behavior. This magnitude ranges from 0.2 to 2.0 times the elastic volumetric strain that would have occurred if the rock were simply elastic (Brace et al., 1966; Paterson & Wong, 2005). Positive dilatancy, associated with volume increase, is linked to the opening of microcracks (Hallbauer et al., 1973), whereas negative dilatancy, or compactancy, is linked to pore collapse and grain crushing (Sulem & Ouffroukh, 2006). With increasing confining pressure, the stress at which dilatancy initiates becomes a progressively larger fraction of the peak and it is more difficult to reach a state of dilatant behavior (Schock et al., 1973). However, it is unclear if the magnitude of dilatancy decreases with confining pressure or is independent of confining pressure, especially in sandstones (Paterson & Wong, 2005).

The dependence of porosity changes during deformation on confining pressure have been documented by CT and SEM analyses of samples after triaxial experiments (Alikarami et al., 2014; Alshibli & Hasan, 2008; Bésuelle et al., 2000; El Bied et al., 2002; Feng et al., 2004; Salvatore et al., 2016; Sulem & Ouffroukh, 2006). For example, CT scans of a core sample of the Vosges sandstone revealed the formation of a distinct, dilated shear band after a triaxial experiment at 30 MPa confining pressure (Bésuelle et al., 2000). SEM images of subsamples of the CT-scanned core sample revealed an increase in the porosity of the shear band; the initial porosity was 22%, and the postexperiment porosity in the shear band was 38%. When the confining pressure was increased to 50 MPa, a less defined, compacted shear band was observed (Bésuelle et al., 2000). Additionally, the shear band formed at 50 MPa was more heterogeneous, exhibiting local zones of compaction and dilation (Bésuelle et al., 2000). Similar results were observed in SEM images of Fontainebleau sandstone (El Bied et al., 2002; Sulem & Ouffroukh, 2006). Dilation within the shear zone was attributed to intergranular and intragranular cracking (Bésuelle et al., 2000), while compaction was attributed to grain reorganization (Bésuelle et al., 2000), as well as grain crushing and pore collapse (Sulem & Ouffroukh, 2006). Other CT studies have documented the entire damage evolution process in sand, showing that shear and volumetric strains evolve in different ways depending on confining pressure (Alikarami et al., 2014; Salvatore et al., 2016). At relatively low confining pressures, a clear dilatant band develops early at 3.9% axial strain, while at relatively high confining pressures, a narrow compactive band with crushed material develops at 7.7% axial strain (Alikarami et al., 2014). Although these observations have constrained porosity evolution during brittle failure, none of these studies provide insights into the spatial distribution of stress within the sample during deformation, or its relationship with volume and porosity variations.

Discrete numerical modeling provides a unique tool to study the micromechanics of brittle rock deformation in exquisite detail, in particular, to track spatial variability of properties and correlations between stress and porosity during deformation (Antonellini & Pollard, 1995; Jiang et al., 2011; Jiang, Liu, et al., 2013; Jiang et al., 2015). For example, numerical shear box experiments by Antonellini and Pollard (1995) show that deformation in a loosely packed, poorly sorted specimen occurs by relative movement of particles, whereas tightly packed, well-sorted specimens develop dilatant zones that develop into discrete faults. Jiang, Zhang, et al. (2013) conducted numerical biaxial experiments and demonstrated that the principal stress vectors rotate in response to porosity increases within the shear band. However, none of these simulations quantified the evolution of stresses and porosity during fracture formation and growth, which DEM simulations are ideally suited to do. This is of particular interest in samples that are deformed under relatively high confining pressures and undergo a bulk decrease in porosity prior to failure (Alikarami et al., 2014; Bésuelle et al., 2000; Handin et al., 1963; Sulem & Ouffroukh, 2006). Here we use 2-D DEM simulations of biaxial experiments to study the micromechanical evolution of rock fracture and the correlations among confining pressure, porosity, and strain, both at the bulk scale and the grain scale. Specifically, we address (1) the coevolution of stress, porosity, volumetric strain, and distortional (shear) strain during different stages of deformation and (2) the effects of confining pressure on the observed micromechanisms. We choose to use 2-D simulations in this study, because they capture the essence of the bulk behaviors of interest that are comparable to laboratory experiments, and significantly reduce computational time. Our simulations do not include pore fluids, and so do not explore the effects of pore pressure evolution on the fracturing process.

**Table 1**  
Particle, Interparticle Bond, and Configuration Properties for T2 Series Simulations

Particle properties		Interparticle bond properties		Configuration properties	
Shear modulus (MPa)	2.9E4	Young's modulus (MPa)	200	Particle radius (mm)	0.15–0.20
Poisson's ratio	0.2	Shear modulus (MPa)	200	Lateral domain (mm)	80 by 40
Friction coefficient	0.3	Tensile strength (MPa)	40	Time step (s)	1.25E – 8
Density (kg/m <sup>3</sup> )	2,500	Cohesion (MPa)	80	No. of particles	11,880

### 3. Methods

#### 3.1. Discrete Element Method (DEM)

The DEM is a particle-based numerical method used to solve Newton's equations of motion for every particle in a particle assemblage (Cundall & Strack, 1979; Morgan, 2015). Particle displacements and forces in response to a displacement boundary condition can be calculated (Morgan, 2015). The normal and shear forces on the particle surfaces are calculated based on a nonlinear Hertz-Mindlin contact theory (Guo & Morgan, 2007; Morgan, 2015). In the absence of bonds, the maximum shear force ( $f_s^{\max}$ ) that can be attained depends on the coefficient of friction at the particle contact ( $\mu_p$ ) and the normal force ( $f_n$ ),

$$f_s^{\max} = \mu_p f_n \quad (2)$$

When  $f_s^{\max}$  is attained, slip occurs. Coordinated particle sliding can result in the formation of a discrete fracture. Bonds can be assigned between particles to impart cohesion. In these simulations, bonds are defined between particles as elastic cylinders that connect particle centers (Morgan, 2015). Bond forces depend on the displacements between particles but are limited by predefined tensile and shear strengths of the bond scaled by area of the bond. The net force on a particle centroid is evaluated by summing all contact forces acting on that particle. The force and displacement equations in the DEM are implemented using RICEBAL (Morgan, 2015), which is based on TRUBAL, an earlier open-source code (Cundall & Strack, 1979).

#### 3.2. Biaxial Experimental Set-Up

We carried out 11 biaxial simulations on identical numerical materials, all consolidated to 10 MPa vertical stress, then deformed biaxially under different confining pressures. Particle and interparticle bond parameters used for our simulations, referred to as the T2 series, are shown in Table 1. The particle and interparticle bond parameters for our material were selected such that they yield bulk mechanical properties of a low strength sandstone (Chang et al., 2006), herein referred to as a low cohesive sandy sediment. For our numerical experiments, we generated ~24,000 particles within particle-based walls in a 160 mm by 80 mm spatial model domain. To prepare the numerical samples, two horizontal confining walls, constructed of rows of particles fixed relative to each other, were moved inward between two vertical walls of particles until the 10 MPa vertical consolidation stress was attained. This initial consolidation represents a simple burial loading (Maltman et al., 1994), which leads to a closer packing of particles and dictates the initial porosity of the sample. After consolidation, the lateral domain of the sample was 80 mm by 40 mm in size (Figure 1). The particles in the horizontal confining walls were then allowed to move independently in the vertical direction while maintaining their constant inward directed stress, thus defining a flexible "membrane" to confine the sample during biaxial compression. Axial compression was initiated by capturing particles within the vertical walls bounding the preconsolidated domain, defining lateral platens, and moving them inward at a constant velocity until the sample failed and beyond (Figure 1). The biaxial experiments were run under confining pressures ranging from 0.1 to 80 MPa. Each biaxial simulation was sampled at increments of 4,000 cycles associated with axial strain increments of 0.01 and relative platen displacements of 0.08 mm.

Our DEM simulations allow us to analyze the responses of identical samples to different confining pressures. This is advantageous to laboratory experiments in which natural sample heterogeneity can cause variations in the results that are difficult to distinguish from other factors. By removing the uncertainties arising from sample heterogeneity, DEM simulations allow us to isolate the precise controls on the fracture process in these systems, and in particular, the specific effects of confining pressure.

### 3.3. Quantifying Stress, Porosity, and Strain

We documented the progressive evolution of each sample during the simulations at two different scales: (1) at the sample scale to evaluate bulk quantities and (2) at smaller scales within the sample by mapping the spatial field of the quantity of interest; the scale of these observations depends on the property being studied. The bulk scale quantities can be directly related to laboratory-scale measurements, whereas the spatial maps of properties yield important new insights into how those properties are distributed across the sample.

Bulk scale properties were obtained from measurements of boundary stresses, boundary positions, and sample volume. As noted above, the membrane stresses are maintained nearly constant at a specified confining pressure; the platen stresses are calculated by summing the net forces of the particles that define each platen and dividing the sum by the area of the platen. Membrane and platen boundary stresses correspond to the minimum and maximum principal stresses ( $\sigma_3$  and  $\sigma_1$ ), respectively, in a laboratory experiment. Note, however, that the membrane stress initially corresponds to  $\sigma_1$  during the initial consolidation, until the platen stress exceeds it during biaxial deformation. A scaled differential stress, referred to as  $\tau_{\max}$ , is presented here,

$$\tau_{\max} = \frac{1}{2}(\sigma_1 - \sigma_3) \quad (3)$$

The displacements of the platens are used to calculate the bulk sample axial strain ( $\epsilon_a$ ). The volume of the sample is calculated from the polygon defined by the boundary particle centers, which allows us to calculate the bulk volumetric strain ( $\epsilon_v$ ). The bulk porosity and its complement, bulk particle abundance, are calculated from the total volume of the domain and the total volume of all the spheres within the sample corrected for the particle overlap volume.

Spatial distributions of properties were analyzed using derived 2-D stress, strain, and porosity fields across the sample. Local stress tensors were calculated by summing the normalized directional components of all the contact forces acting on each particle within a grid element (Morgan, 2015), here set to 1 mm by 1 mm. A 2-D map of  $\tau_{\max}$ , an invariant quantity, is derived from the local stress tensors. Two-dimensional maps of particle abundance within a 1 mm by 1 mm grid element are also calculated,

$$\text{Porosity (\%)} = 100\% - \text{Particle abundance (\%)} \quad (4)$$

Two-dimensional volumetric strain and distortional strain over a domain are derived from local strain tensors calculated from particle displacements (Morgan, 2015) on a finer grid of 0.32 mm by 0.32 mm. Distortional strain is the second invariant of the deviatoric strain tensor. The derived stress, porosity, and strain fields are plotted using Generic Mapping Tools (Wessel & Smith, 1995).

## 4. Results

### 4.1. Changes in Bulk Stress and Porosity

To examine the coevolution of bulk properties during biaxial deformation, we examine the results of a representative test carried out at 5 MPa confining pressure (Test T2-05; Table 2). We document evolution of the bulk sample  $\tau_{\max}$  and porosity at 5 MPa confining pressure with axial strain. For Test T2-05,  $\tau_{\max}$  increases from an initial value of 1.9 MPa, attains a peak of 48.2 MPa, and then drops to a value of about 20 MPa with increasing  $\epsilon_a$  (Figure 2a). A similar trend in  $\tau_{\max}$  is observed when plotted against  $\epsilon_v$ ; however, volumetric strain initially increases from zero to 1.3% (compaction) and is followed by a decrease to a negative value of  $-1.9\%$  (dilation). Porosity decreases from an initial value of 16.3% to a minimum of 15.2% and then increases to 17.9% with increasing  $\epsilon_a$  (Figure 2a). The observed  $\tau_{\max}$ - $\epsilon_a$  pattern is consistent with similar laboratory compression tests (e.g., Bésuelle et al., 2000; El Bied et al., 2002; Sulem & Ouffroukh, 2006). On that basis, we identify four representative points (i, ii, iii, and iv) that denote key changes in bulk  $\tau_{\max}$  and porosity for Test T2-05. Point i represents preyield elastic loading of the sample; points ii and iii represent yield of the sample; points ii and iii represent yield and peak stresses, respectively; and point iv represents a postpeak condition (Figure 2a). The phases of deformation can be represented by stress-strain slope behavior,  $d\tau_{\max}/d\epsilon_a$  and  $d\tau_{\max}/d\epsilon_v$  (Figures 2b and 2c). When axial compression begins, the increasing stress is transmitted through the material from the platens. This can be thought of as an “initializing” phase for the numerical set-up during which both  $d\tau_{\max}/d\epsilon_a$  and  $d\tau_{\max}/d\epsilon_v$  are increasing (Figures 2b and 2c). After this initial increasing



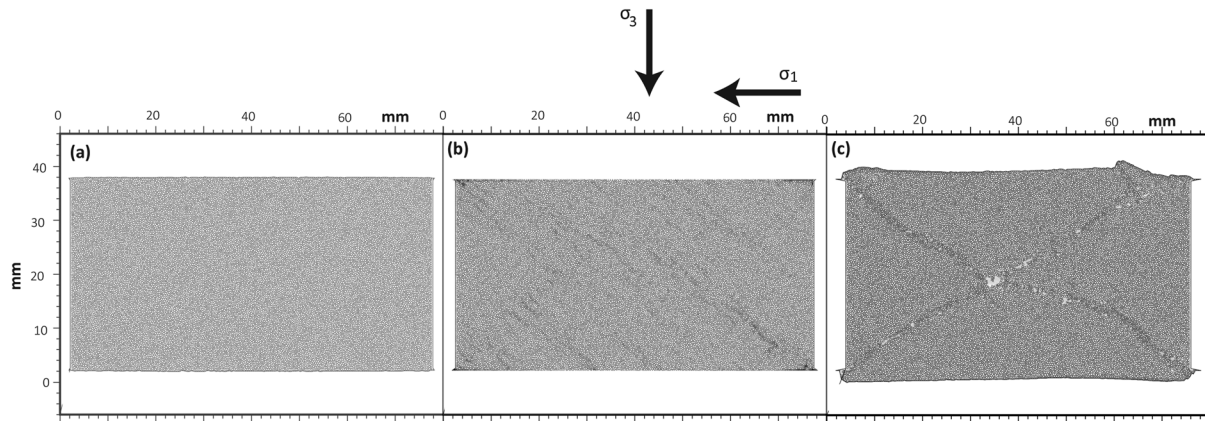


**Figure 1.** Particle configurations of Sample T2-05 prior to and during biaxial compression. (a) Sample preconsolidated to 10 MPa, representing the starting configuration for all simulations. (b) Sample deformed by biaxial compression in horizontal direction under a vertical confining pressure ( $\sigma_3$ ) of 5 MPa; 3.6% axial strain, at the onset of failure. The  $\sigma_3$  is initially horizontal during initial consolidation but rotates to a vertical stress when the stress on the horizontal walls is exceeded by that on the vertical during biaxial compression. (c) Biaxially deformed sample in (b) at 6.63% axial strain; through-going conjugate shear fractures have developed.

portion of the stress-strain curves,  $d\tau_{\max}/d\epsilon_a$  and  $d\tau_{\max}/d\epsilon_v$  start decreasing until the onset of negative dilatancy. At the onset of dilatancy,  $d\tau_{\max}/d\epsilon_v$  first starts to increase (Figure 2b) as previously noted by others (Brace et al., 1966; Hoek & Martin, 2014), while  $d\tau_{\max}/d\epsilon_a$  shows little variability (Figure 2c). The onset of negative dilatancy occurs at 0.70%  $\epsilon_v$  (Figures 2a and 2b). Point i is picked after the onset of negative dilatancy. It occurs at  $\tau_{\max}$  of 35.8 MPa and  $\epsilon_a$  of 1.87% during the linear stage of deformation, which persists until yield (Figure 2a). The yield point (point ii) is picked where the slope of the stress-axial strain curve starts to decrease (Figure 2c), corresponding to the onset of strain hardening (Jaeger et al., 2007). The yield stress of 43.4 MPa occurs at a  $\epsilon_a$  of 2.38% and coincides with the minimum porosity of 15.2% (Figure 2a). Peak stress (point iii), signifying the onset of macroscopic failure, occurs at a  $\tau_{\max}$  51.6 MPa and a  $\epsilon_a$  of 4.60% (Figure 2a). Strain softening follows peak stress, corresponding to increasing porosity. Point iv is representative of postpeak conditions at a  $\tau_{\max}$  of 22.5 MPa and a  $\epsilon_a$  of 6.63% (Figure 2a).

#### 4.2. Microstructural Evolution of Stress, Porosity, and Strain

To better understand the micromechanical behavior of our numerical material during deformation, we plot the spatial distributions of  $\tau_{\max}$ , volumetric strain, distortional strain, and porosity at points i through iv. We first look at Test T2-05 in detail (Figure 3). Overall, the spatial maps of each property evolve from relatively homogeneous at the start of the test (point i) to very heterogeneous leading up to and following failure (point iv). We examine each property's evolution in more detail below and then discuss correlations among them. The spatial distribution of  $\tau_{\max}$  is relatively homogeneous prior to peak stress, encompassing the elastic loading phase and yield, and becomes very heterogeneous after peak stress (Figure 3a). Due to the granular nature of our material, stress is transmitted across the sample by particle chains that support high forces, referred to as stress chains (Howell et al., 1999; Peters et al., 2005; Zuriguel & Mullin, 2008). The result is a complex network of high stresses that evolve as the sample deforms. This network is relatively homogeneous throughout the sample prior to peak stress but gradually localizes, especially along the sample boundaries, after peak stress (Figure 3a). To highlight the increasing heterogeneity of stress during brittle failure, we

**Table 2**  
Bulk Stress ( $\tau_{\max}$ ) Data for T2 Series Experiments

Test name	Confining pressure (MPa)	$\tau_{\max}$ initial (MPa)	Linear elastic $\tau_{\max}$ - $\epsilon_a$ slope	$\epsilon_a$ at yield (%)	$\tau_{\max}$ at yield (MPa)	$\epsilon_a$ at peak (%)	$\tau_{\max}$ at peak (MPa)	$\tau_{\max}$ residual (MPa)	$\tau_{\max}$ drop (MPa)
T2-05	5	1.9	15.6	2.38	43.4	3.11	48.2	19.7	28.5
T2-10	10	0.1	17.1	2.38	44.9	3.63	51.6	23.0	28.6
T2-20	20	3.9	18.7	2.69	46.9	3.84	56.3	32.2	24.1
T2-30	30	7.6	19.5	2.90	52.0	4.25	59.7	36.4	23.3
T2-40	40	11.4	19.8	3.52	59.0	4.77	64.3	40.9	23.4

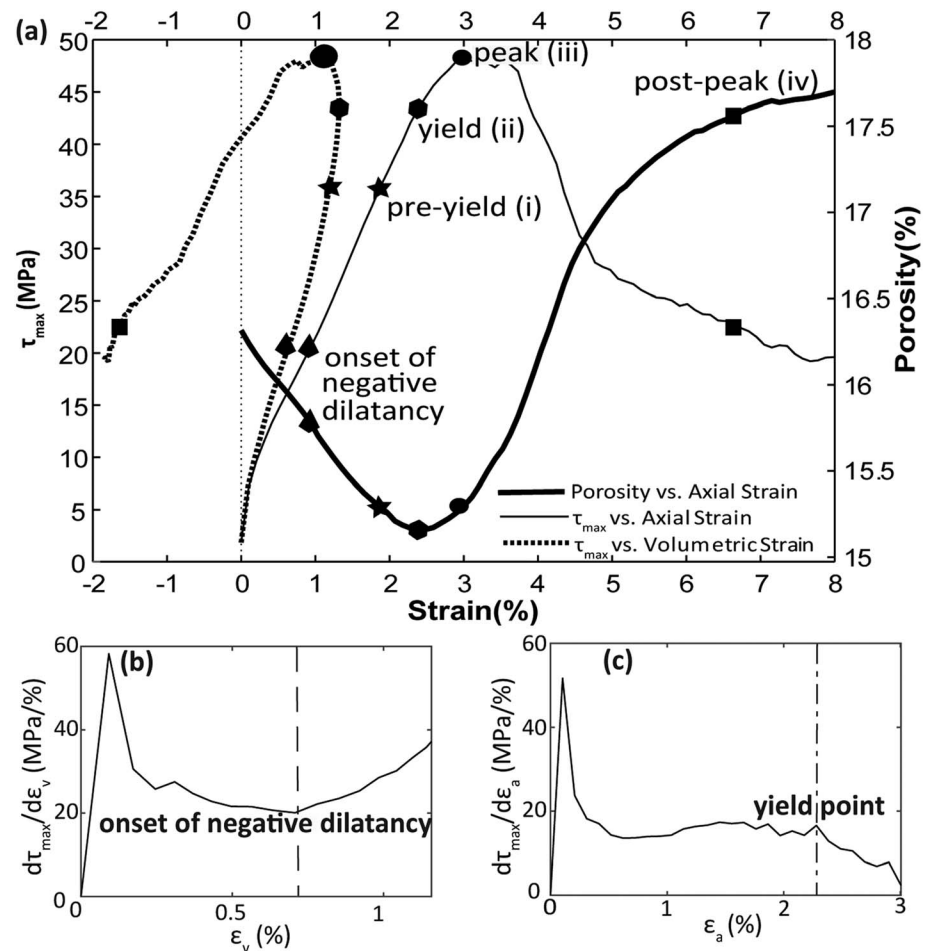


**Figure 2.** (a) Maximum shear stress,  $\tau_{\max}$ , and sample porosity as a function of strain for Test T2-05. The black shapes on the plots correspond to significant stages of deformation. (b) Evolution of slopes of  $\tau_{\max}$  versus  $\varepsilon_v$  plot for Test T2-05, used to identify onset of negative dilatancy during the biaxial compression—the onset of negative dilatancy corresponds to a local slope minimum. (c) Evolution of slopes of  $\tau_{\max}$  versus  $\varepsilon_a$  plot for Test T2-05, used to identify yield during the biaxial compression—yield occurs when the slope decreases measurably.

construct a binary stress map (Figure 4), applying a threshold of the spatially averaged, particle-based  $\tau_{\max}$  plus two standard deviations. Stress values greater than the threshold  $\tau_{\max}$  constitute the strong network and are depicted in black. During the linear elastic phase,  $\tau_{\max}$  is characterized by closely spaced, anastomosing stress chains that distribute the boundary stresses across the sample (Figure 4a; point i); 47.0% of the particles in the sample constitute the strong network (Table 3). The anastomosing character of the high stress chains is still evident at yield stress (Figure 4a; point ii); however,  $\tau_{\max}$  has increased over the sample domain, consistent with the higher stresses acting on the sample (Figure 3a; point ii). At peak stress, the standard deviation in particle  $\tau_{\max}$  increases to 55.2%, which exceeds the value 51.8% at yield stress reflecting increased heterogeneity at the onset of failure (Figure 4b, points ii and iii, and Table 3). Postyield stress heterogeneity across the sample is quite extreme; a region of low stress has developed in the center of the sample, and is surrounded by very few high stress chains that span the sample (Figure 4a, point iv). At this point, fewer particles constitute the strong network, as reflected by the increase in the standard deviation to 73.0% (Figure 4b, point iv, and Table 3).

Concurrent with progressive changes in stress distribution within the sample during deformation, volumetric strain evolves from relatively uniform compaction across the entire sample to localized zones of dilation along discrete bands (Figure 3b). Preyield, the sample has compacted slightly (Figure 3b, point i). By yield stress, localized dilation along short, discontinuous bands with conjugate orientations (Figure 3b, point ii) exists. At this point, these dilational bands have an average length of 7.5 mm and are oriented at an angle

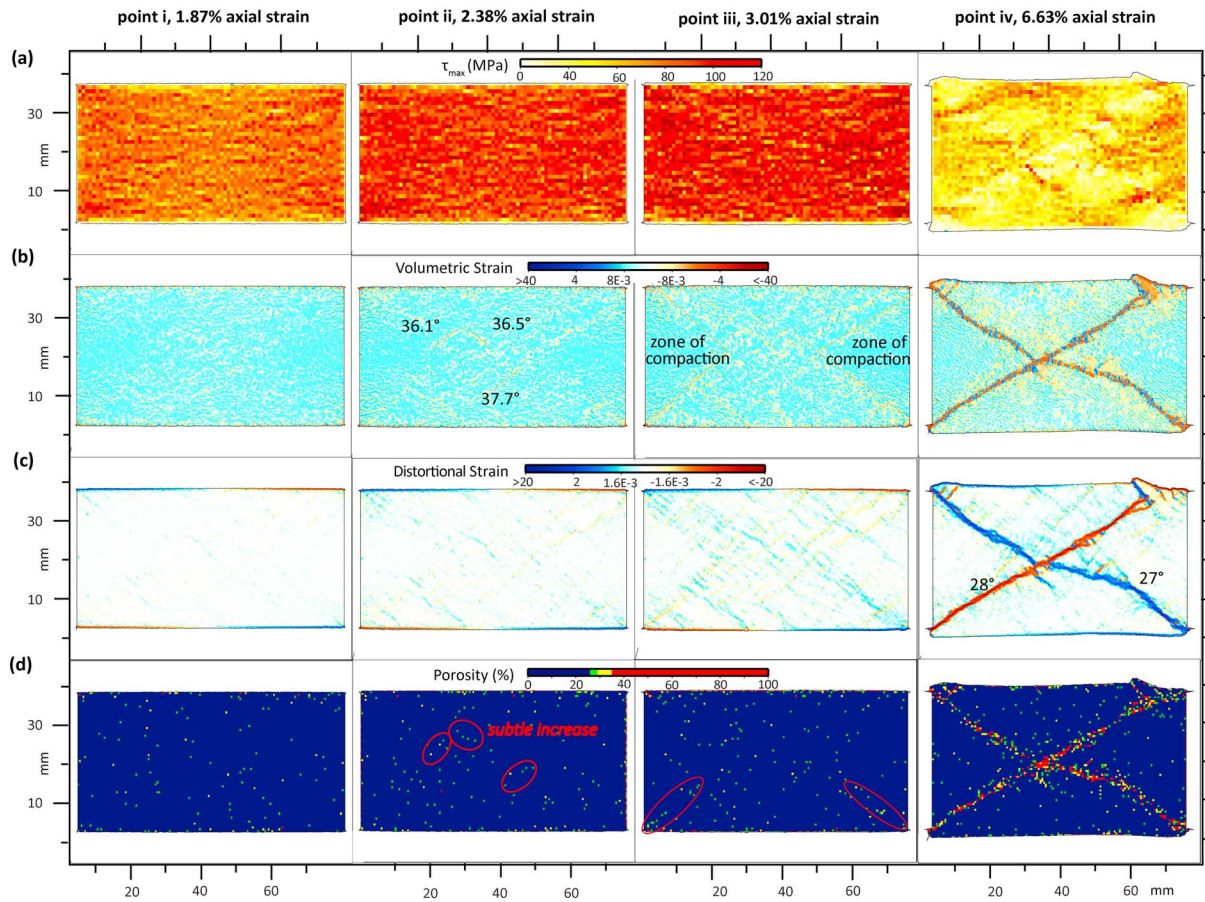


**Figure 3.** Progressive evolution of spatial distribution of sample properties and strains with axial strain for Sample T2-05 at significant points during deformation, i-iv as shown in Figure 2. (a) Evolution of  $\tau_{\max}$ . (b) Evolution of volumetric strain. The red color and negative values represent dilation, while the blue color and positive values represent compaction. (c) Evolution of distortional strain. Distortional strain also records sense of shear; that is, the red color and negative values are top-to-right (right-lateral) and the blue color and positive values are top-to-left (left-lateral). (d) Evolution of porosity.

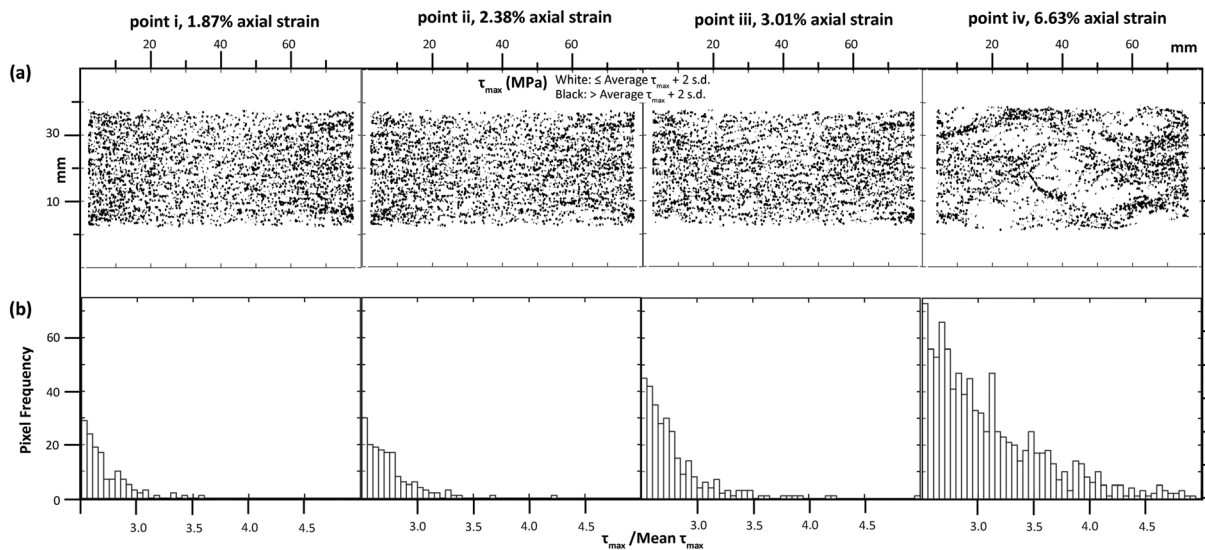


**Figure 4.** (a) Binary map highlighting spatial distribution of  $\tau_{\max}$  values greater than average plus two standard deviations for Sample T2-05 at significant points during deformation, i-iv in Figure 2. (b) Corresponding histogram of the spatial distribution of  $\tau_{\max}$  in (a), normalized by the mean  $\tau_{\max}$ , showing evolution from relatively homogeneous to highly heterogeneous with increasing axial strain.



**Table 3**  
Microstructural Stress ( $\tau_{max}$ ) Data for T2 Series Experiments

Confining pressure (MPa)	Point ii—yield point		Point iii—peak stress		Point iv		
	% Standard deviation	% Black pixels	% Standard deviation	% Black pixels	% Standard deviation	% Black pixels	No. of distinct stress chains across fracture
5	51.8	47.0	55.2	46.3	73.0	42.2	8
10	50.3	47.3	58.2	45.4	75.1	41.3	6
20	50.7	47.0	57.3	45.3	70.4	41.7	3
30	51.4	46.9	58.1	45.3	67.3	41.9	3
40	53.8	46.1	59.0	44.9	65.7	43.0	2

of  $\sim 37^\circ$  from  $\sigma_1$  (Figure 3b, point ii). By peak stress, the number of dilational bands has increased, and they outline two triangular-shaped zones of compaction next to the platen boundaries (Figure 3b, point iii). Some of the dilational bands remain small and dispersed within the sample. Postpeak dilation is highly localized along two through-going conjugate dilational zones oriented at angles of  $28^\circ$  and  $27^\circ$  relative to  $\sigma_1$ , corresponding to brittle fractures (Figure 3b, point iv).

The distortional strain field, by comparison, evolves more subtly with increasing axial strain during the experiment (Figure 3c). At yield, indistinct zones of distortional strain are evident (Figure 3c, point ii). By peak stress, a left-lateral shear band is evident at the bottom right of the sample and a right-lateral shear band at the bottom left (Figure 3c, point iii). The magnitude of distortional strain at these points averages  $\sim 1.6\epsilon - 3$ . By point iv, distortional strain is highly localized into the two fractures identified in the volumetric strain plots, and the average magnitude of distortional strain at the lower corners has increased to 2.0. Now the two through-going conjugate shear bands span the entire domain (Figure 3c, point iv).

Porosity, which is related to the volumetric strain, is relatively uniform across the domain of the sample at the outset but also exhibits local changes during the biaxial test. During the linear elastic phase, the porosity field remains relatively uniform at an average spatial porosity of  $\sim 20\%$  (Figure 3d, point i). This uniform porosity distribution persists until yield, by which point the sample experiences a subtle increase of about 5% in porosity in few localized regions (Figure 3d, point ii). By peak stress, porosities at the lower left and right corners have reached  $\sim 30\%$  (Figure 3d, point iii). From this point on, porosities increase locally, creating distinct zones of higher porosity that correspond to the brittle fractures (Figure 3d, point iv); however, not all localized zones of higher porosity turn into the dominant fracture (Figure 3d, points iii to iv).

To understand how changes in stress, strain, and porosity are correlated, we compare the spatial distributions of stress, volumetric strain, distortional strain, and porosity for Test T2-05. During the linear elastic stage, the relatively uniform porosity across the sample corresponds to high stress, and sample-wide compaction. Distortional strain within the sample is not evident at this point (Figures 3a–3d, point i). At yield, the spatial distributions of stress, volumetric strain, and distortional strain are still relatively uniform; however, dilational bands are starting to develop, apparently overcoming the resisting stresses holding the bands closed (Figures 3a to 3d, point ii). As peak stress is approached, more dilational bands develop, some associated with minor distortion. The stress and porosity fields at this point are still relatively uniform (Figures 3a–3d, point iii), indicating that dilation is occurring at a scale that would be difficult to observe in natural samples. Following peak stress, two through-going shear fractures develop by the coalescence of the more distributed deformation bands. These fractures correspond to distinct zones of higher porosity, generally lower stresses, highly localized dilation, and significant distortional strain (Figures 3a–3d, point iv). Localized high stress chains occur across the fracture zone corresponding to localized zones of low porosity (Figures 3d and 4a, point iv).

#### 4.3. Effect of Confining Pressure on the Changes in Bulk Stress and Porosity

As has been noted from laboratory studies (e.g., Bésuelle et al., 2000; El Bied et al., 2002; Sulem & Ouffroukh, 2006), confining pressure influences trends in  $\tau_{max}$  and porosity. For example, biaxial compression tests on the other T2 series show similar  $\tau_{max}-\epsilon_a$ , porosity- $\epsilon_a$ , and  $\tau_{max}-\epsilon_v$  behavior as for Test T2-05; however,  $\tau_{max}$  at yield and at peak both increase with increasing confining pressure (Figure 5a) while the minimum porosity and porosity at peak stress both decrease with increasing confining pressure (Figure 5b). The axial and volumetric strains at yield stress, peak stress, and minimum porosity increase with increasing confining pressure (Figure 5c).

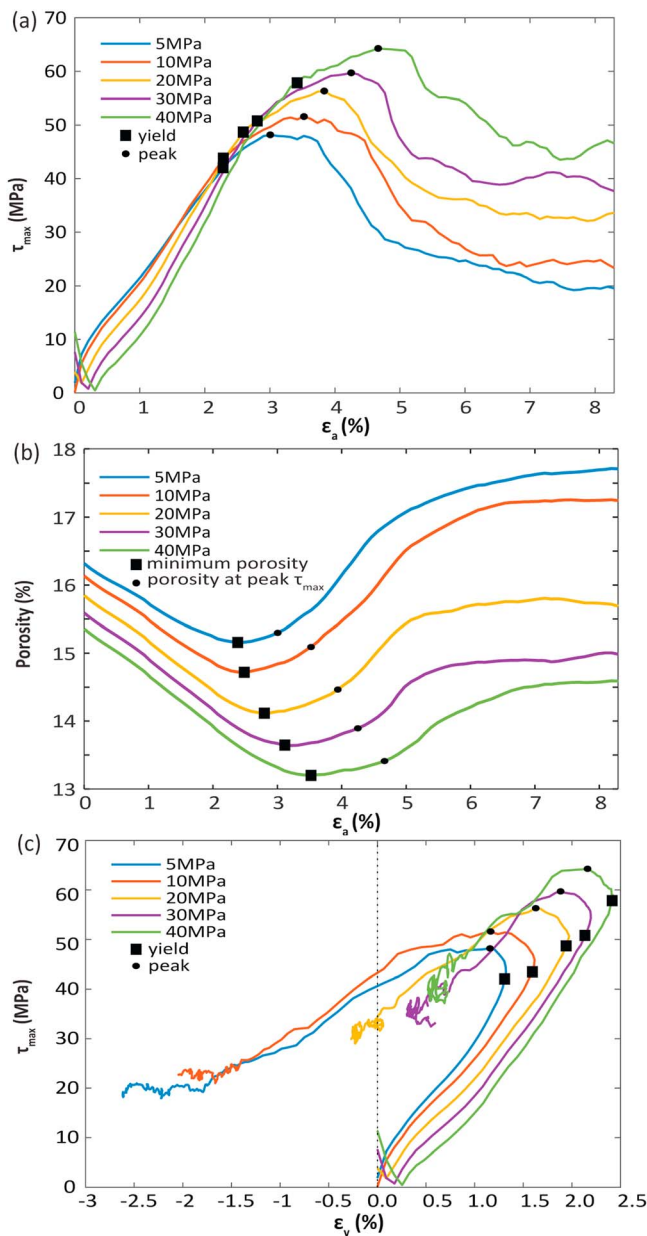


**Figure 5.** (a) Plots of  $\tau_{\max}$ - $\epsilon_a$  for biaxial compression tests at different confining pressures. Yield and peak stress and the strain at which they occur increase with increasing confining pressure. (b) Plots of Porosity- $\epsilon_a$  for biaxial compression tests at different confining pressures. Minimum porosity and the porosity at peak stress decrease with increasing confining pressure. (c) Plots of  $\tau_{\max}$ - $\epsilon_v$  for biaxial compression tests at different confining pressures. Samples settle out at final  $\tau_{\max}$  values, which fluctuate about a constant mean, at a volumetric strain that is less than zero for T2-05, T2-10, and T2-20 but greater than zero for T2-30 and T2-40.

Increasing confining pressure influences the general trends observed in the  $\tau_{\max}$ - $\epsilon_a$  data especially at the initial stage of the experiment (Figure 5a and Table 2). In Tests T2-20, T2-30, and T2-40, which span higher confining pressures (Table 2),  $\tau_{\max}$  shows an initial drop followed by an increase (Figure 5a). This stress drop is not evident in Tests T2-05 and T2-10. The initial drop results from the switch in orientation of  $\sigma_1$  from vertical (membrane stress) to horizontal (platen stress). Because the biaxial experiment starts from the configuration state at the end of vertical consolidation,  $\tau_{\max}$  is initially nonzero (Table 2) and  $\sigma_1$  is vertical. As the platens start to move inward, the horizontal stress increases until it exceeds the vertical stress, rotating  $\sigma_1$  to horizontal. At this stage,  $\tau_{\max}$  starts to increase with a slope that increases slightly with increasing confining pressure until yield (Table 2). The yield and peak stresses and the axial strains at which they occur increase linearly with confining pressure (Figures 6a and 6b), although the linear fit is better at peak stress and strain ( $r^2 = 0.9916, 0.9657$ , respectively) compared to yield stress and strain ( $r^2 = 0.9464, 0.9285$ , respectively). After peak stress,  $\tau_{\max}$  decreases until it reaches its residual value. This decrease in stress also decreases with increasing confining pressure (Table 2).

Porosity trends during each biaxial experiment also vary systematically as a function of confining pressure (Figure 5b and Table 4). Confining pressure influences initial porosity, which is highest for the lowest confining pressures (Figure 5b). For each experiment, porosity decreases to a minimum value; the strain at which the minimum porosity occurs increases linearly with increasing confining pressure (Figures 6c and 6d and Table 4). As porosity starts to increase again, the porosity curves diverge with increasing axial strain. For confining pressures greater than 30 MPa, the final porosity of the samples is less than the initial porosity; at lower confining pressures, the final porosity is greater than the initial porosity (Figure 5b).

Confining pressure also influences the trends in the  $\tau_{\max}$ - $\epsilon_v$  plots, which resemble the  $\tau_{\max}$ - $\epsilon_a$  plots until the yield point (Figures 5a and 5c). Again,  $\tau_{\max}$  shows an initial drop followed by an increase in Tests T2-20, T2-30, and T2-40 (Figure 5c). The onset of dilatancy occurs at  $\sim 0.74\%$   $\epsilon_v$ , irrespective of confining pressure (Table 5). At yield, the bulk volumetric strain starts to decrease. The volumetric strain at yield also increases with increasing confining pressure (Figure 5c). The magnitude of dilatancy, determined as the maximum departure of the stress-volumetric strain curve from the line representing elastic behavior, increases with increasing confining pressure (Figure 5c and Table 5). As the volumetric strain continues to decrease, the final volumetric strain is less than zero for T2-05, T2-10, and T2-20 (Figure 5c) indicating a bulk dilation of the sample, but greater than zero for T2-30 and T2-40 (Figure 5c) indicating a bulk compaction.

#### 4.4. Effect of Confining Pressure on Microstructural Evolution of Stress, Porosity, and Strain

Given the observed differences in bulk properties for samples deformed under different confining pressures, the microstructural evolution of these samples during brittle fracturing is expected to vary as well. Interestingly, although the magnitude of  $\tau_{\max}$  across the samples increases with increasing confining pressure, the spatial distribution of  $\tau_{\max}$  prior to peak stress remains relatively uniform regardless of confining pressure, yielding a standard deviation of around 52% (Table 3). The stress chains that

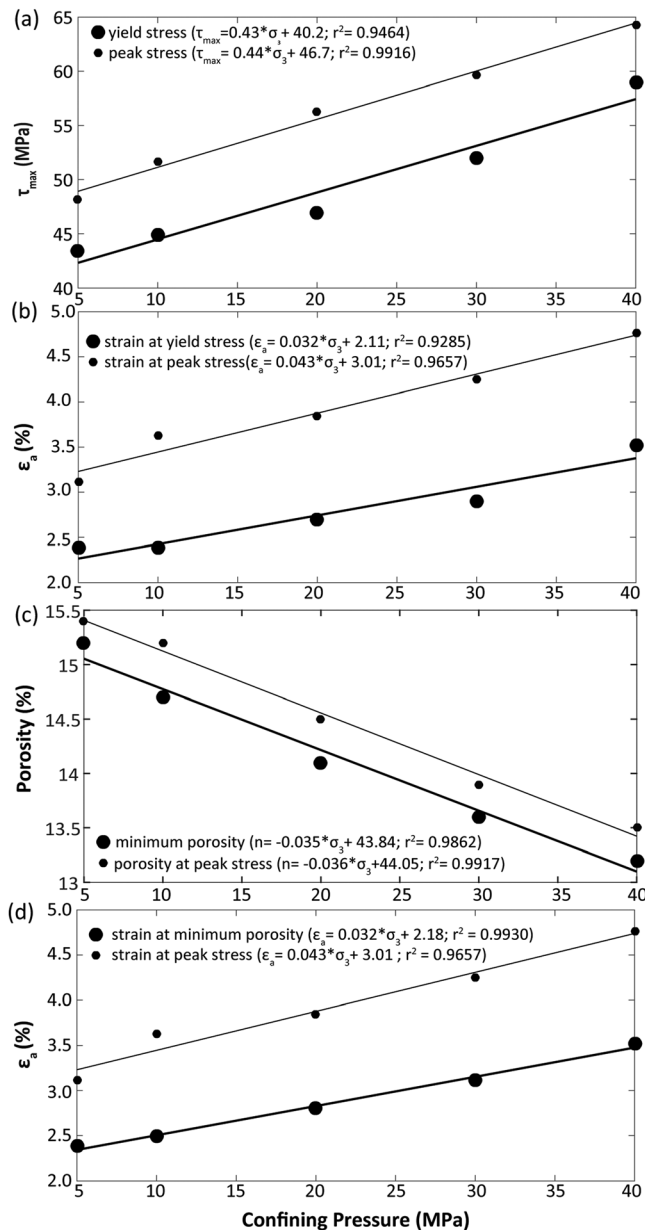


**Figure 6.** (a) Values of  $\tau_{max}$  at yield and peak stress versus confining pressure. (b) Axial strain corresponding to yield and peak stress versus confining pressure. (c) Minimum porosity and porosity at peak stress versus confining pressure. (d) Axial strain corresponding to minimum porosity and porosity at peak stress versus confining pressure. All functions show approximately linear relationships with confining pressure.

## 5. Discussion

Our 2-D numerical biaxial simulations produce bulk behaviors and brittle deformation that are characteristic of 3-D sediments and sandstones deformed in the laboratory. For example, our stress-strain plots show a linear elastic phase, yield, strain hardening to failure, and strain softening before attaining a residual strength, as has been previously observed (Alikarami et al., 2014; Bésuelle et al., 2000; Paterson & Wong, 2005; Wong et al., 1997). From the porosity-strain plots, we see an initial reduction to a minimum value followed by increasing porosity to a residual value, which is also consistent with laboratory experiments (Handin et al., 1963; Wong et al., 1997). The residual value of porosity is influenced by confining pressure; for confining pressures less

constitute the strong network at this stage of deformation appear to develop similarly, independent of confining pressure; here, the chains constitute about 47% of the particles in the sample at yield (Table 3).

In contrast, the spatial distribution of strain shows a dependence on confining pressure (Figure 7). To compare the spatial distribution of strain at different confining pressures, we create a histogram of the strain pixel frequency within the sample. For the volumetric strain histogram, we bin the strains using an interval of 0.001 and utilize only the negative volumetric strains to highlight dilation within the sample (Figure 7b). Thus, a higher pixel frequency of each volumetric strain bin indicates greater dilation. In contrast, for the distortional strain histogram, we bin the strains using an interval of 0.05 and utilize the absolute value of both positive and negative distortional strains within the sample (Figure 7d). Similarly, a higher pixel frequency of each distortional strain bin indicates greater distortional strain. Our histograms show that dilation at yield is inhibited with increasing confining pressure (5 to 40 MPa; Figure 7a); the frequency of negative volumetric strains between 0 and 0.001 within the sample decreases from ~600 at 5 MPa to ~250 at 40 MPa (5 to 40 MPa; Figure 7b). Although dilation is suppressed at higher confining pressure, the sample experiences distortional strain (5 to 40 MPa; Figure 7c); the frequency of distortional strain between 1.0 and 2.0 increases from 0 at 5 MPa to ~100 at 40 MPa (5 to 40 MPa; Figure 7d).

The variations in stress and porosity distributions are most pronounced postpeak, when the through-going shear bands have developed fully. For example, the steepness of the fracture increases from ~27° to 45° with increasing confining pressure (5 to 40 MPa; Figure 8a and Table 4) while the percentage standard deviation of  $\tau_{max}$  across the fracture decreases with increasing confining pressure (Table 3). The spatial distribution of  $\tau_{max}$  becomes more localized in all samples, but this is most evident at lower confining pressures, which exhibit the highest standard deviation (Figures 9a and 9b and Table 3). Also, the variations in porosity across the fracture decrease with increasing confining pressure (Figure 8b). To look at these porosity variations, we create porosity transects across the middle of the sample at each confining pressure (Figure 8c). These plots allow us to characterize the changes in porosity with respect to the initial average spatial porosity across the sample domain. Most of the porosity increase, with respect to the initial average spatial porosity, experienced by the sample occurs along the fractures (Figures 8b and 8c); however, the magnitude of porosity increase decreases with increasing confining pressure (Figure 8c).

**Table 4**  
Bulk Porosity Data for T2 Series Experiments

Test name	Confining pressure (MPa)	Initial porosity (%)	$\varepsilon_a$ at minimum porosity (%)	Minimum porosity (%)	Decrease in porosity (%)	Residual porosity (%)	$\alpha$ -left (°)	$\alpha$ -right (°)
T2-05	5	16.3	2.38	15.2	1.1	17.9	28	27
T2-10	10	16.1	2.49	14.7	1.4	17.3	42	34
T2-20	20	15.9	2.80	14.1	1.8	15.7	40	40
T2-30	30	15.6	3.11	13.6	2.0	15.0	41	45
T2-40	40	15.4	3.52	13.2	2.2	14.6	45	45

than the consolidation stress we simulate an average porosity increase (dilatant behavior), whereas for confining pressures exceeding the consolidation stress we simulate an average porosity reduction (compactant behavior). These behaviors are also evident from a calculation of the Roscoe angle (Table 6), (Oda & Iwashita, 1990), such that the angle of dilation is positive at lower confining pressures but negative at higher confining pressures. Hence, it appears that increasing confining pressure makes the sample stronger and suppresses dilation. In our simulations, this transition from dilatant to compactant behavior occurs at 20 MPa confining pressure, which is also consistent with the almost zero dilation angle (Table 6), but this is not always the case (Bésuelle et al., 2000; Sulem & Ouffroukh, 2006). Consolidation stress, initial porosity, strain rate, grain-size distribution, and cementation can affect the overall strength and brittle behavior of a material, and thus control the transition from dilatant to compactant behavior. The consolidation stress dictates the initial porosity of the sample, which imposes a control on the strength and volume changes that the material undergoes (Lambe & Whitman, 1969). Additionally, a greater strain rate or cementation increases the strength of a material and vice versa. Our platen velocity of 1.6 m/s, though on the high side of the range typically used in other DEM studies (Ding et al., 2014), still ensures quasi-static loading of the material. Selecting a lower loading velocity results in a slightly lower bulk  $\tau_{\max}$  at peak, and a less gradual strain softening; however, the overall bulk trends are not affected. Although we adequately reproduce the general behavior of natural samples using our 2-D simulations, the actual values calculated for porosity and volume are lower but not unrealistic. This is because we assume a unit z-dimension in our calculations. We are also limited in the resolution of the values calculated by the finite number of particles that we can have in our simulations compared to natural samples. Hence, we acknowledge that our 2-D numerical simulations have limitations and will not give a precise reproduction of lab results. However, through our numerical experiments, we can uniquely probe the spatial variability of stress and porosity within the deforming sample and relate that to the deformation process.

Our microstructural observations during deformation reveal progressive evolution of stress and porosity, from relatively homogeneous prior to peak stress to highly heterogeneous postpeak (Figure 3). This evolution of stress denotes the progressive concentration of stresses into a few high magnitude stress chains as fractures develop (Figure 4). An increase in the percentage standard deviation of  $\tau_{\max}$  between peak and postpeak stress also supports this heterogeneous spatial distribution of stress (Table 3). Postpeak regions of generally lower stresses and higher porosity are spatially correlated (Figures 3a and 3d, point iv). This heterogeneous distribution of stress correlates with the observed decrease in stress and increase in porosity at a decreasing rate especially at lower confining pressures (Figure 5). Clearly, open fractures are controlling the system by reducing the number of effective stress chains, forcing stresses to concentrate in the few

**Table 5**  
Bulk Volumetric Strain Data for T2 Series Experiments

Test name	Confining pressure (MPa)	$\varepsilon_v$ at onset of dilatancy (%)	$\tau_{\max}$ at onset of dilatancy, $\tau_{\max}^P$ (MPa)	Elastic $\varepsilon_v$ , E (%)	$\tau_{\max}$ at peak, $\tau_{\max}^P$ (MPa)	Magnitude of dilatancy, D (%)	$\tau_{\max}^P/\tau_{\max}^P$	D/E
T2-05	5	0.71	22.0	1.97	48.2	0.87	0.45	0.6130
T2-10	10	0.78	21.1	2.30	51.6	1.00	0.41	0.4923
T2-20	20	0.73	16.4	2.63	56.3	1.18	0.29	0.3811
T2-30	30	0.72	13.1	2.88	59.7	1.26	0.22	0.3481
T2-40	40	0.74	9.7	2.99	64.3	1.54	0.15	0.2835



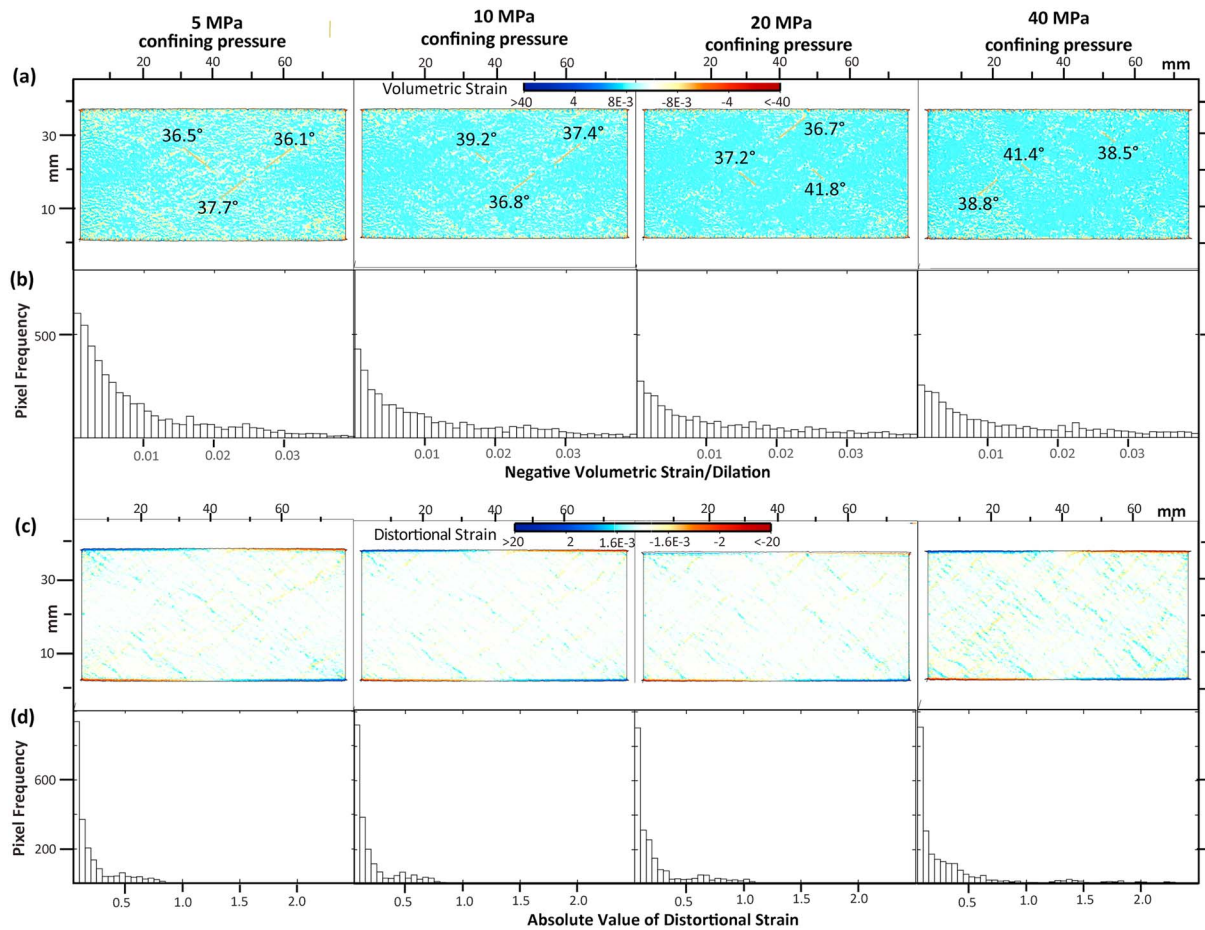


**Figure 7.** (a) Spatial distribution of volumetric strain for T2 series samples deformed under different confining pressures at yield point ii. (b) Histogram showing the pixel frequency of negative volumetric strains in (a). A higher pixel frequency of each volumetric strain bin indicates greater dilation, so, dilation is inhibited with increasing confining pressure. (c) Spatial distribution of distortional strains for T2 series samples deformed under different confining pressures at yield point ii. (d) Histogram showing the pixel frequency of the absolute value of distortional strains in (c). Distortion is promoted with increasing confining pressure.

places where the sample porosity is still low compared to the fracture porosity. This heterogeneous spatial distribution in stress and porosity results from different modes of deformation, which depend on confining pressure.

All our simulations result in two conjugate dominant fractures although the process by which they form and their subsequent evolution depends on confining pressure. We document that dilation is the dominant mode of deformation at relatively low confining pressures, whereas dilation is suppressed, and distortion is favored at higher confining pressures (Figure 7). In our simulations, yield corresponds to the opening of dilational bands, some of which evolve into through-going shear fractures, but only for confining pressures below 20 MPa (5 to 10 MPa; Figures 7a and 7b). This is consistent with previous studies where the yield point is associated with the onset of unstable fracture propagation and grain shattering (Bieniawski, 1967b), as well as the point at which microcracks begin to open (Hallbauer et al., 1973). For confining pressures greater than 20 MPa, the opening of dilational bands does not occur at yield (20 to 40 MPa; Figure 7a) but closer to the peak stress; however, the sample experiences more distortional strain compared to lower confining pressures (20 to 40 MPa; Figures 7c and 7d). Irrespective of the mode of deformation, the coalescence of high angle dilational bands (Figure 7a) eventually leads to the formation of a lower angle fracture (Figure 8a).

Another interesting observation from our simulations is that the fracture angle steepens with increasing confining pressure (Figure 8a and Table 4). Based on a linear Mohr-Coulomb failure criterion, the fracture angle ( $\alpha$ , degrees) is related to the friction angle ( $\phi$ , degrees),

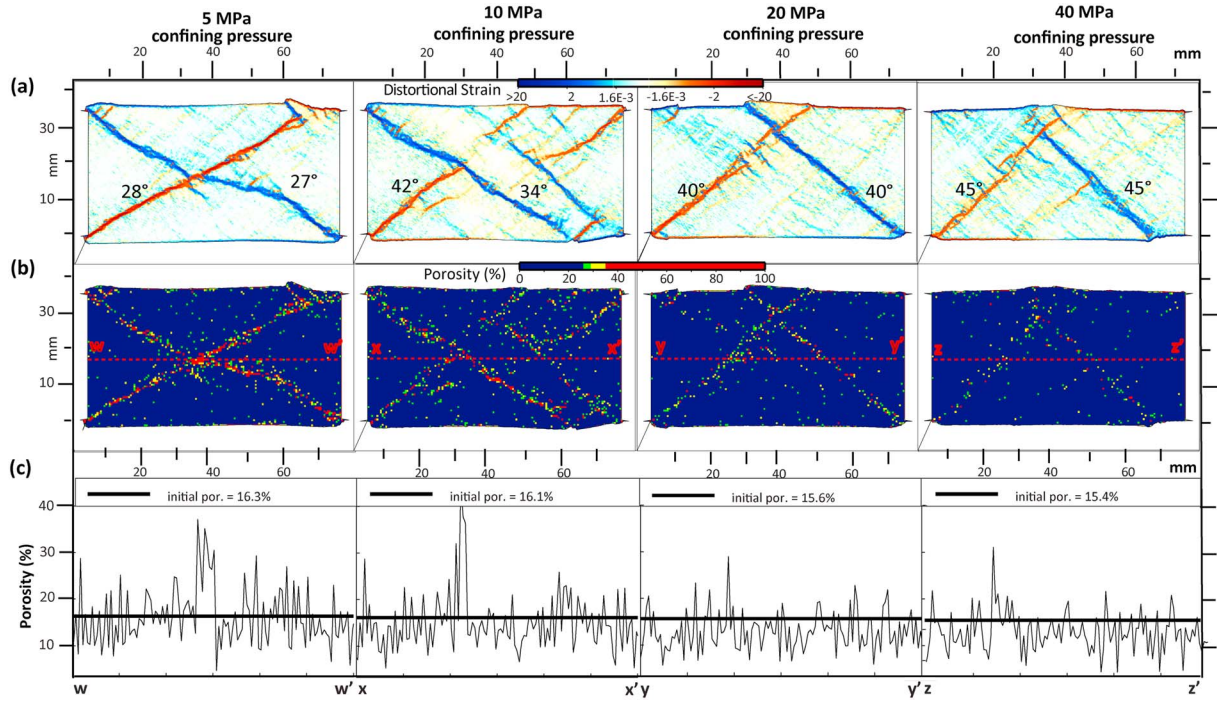


**Figure 8.** (a) Distortional strain and (b) porosity for T2 series samples deformed under different confining pressures after sample failure. Shear fractures correspond to a zone of concentrated distortional strain and locally high porosity. (c) Porosity transect along line shown in (b) shows that dilation is concentrated along the fractures, and suppressed by increasing confining pressure. However, within the sample, compaction occurs at all confining pressures with respect to the average initial porosity of the sample.

$$\alpha = 45^\circ - \phi/2 \quad (5)$$

So the friction angle should decrease with increasing confining pressure. However, a linear Mohr-Coulomb relationship for our material gives us a value of  $18^\circ$  for the friction angle irrespective of confining pressure (Jaeger et al., 2007; Figure 10):

$$\tau \text{ (MPa)} = 0.3294\sigma_n \text{ (MPa)} + 33.325 \text{ (MPa)} \quad (6)$$

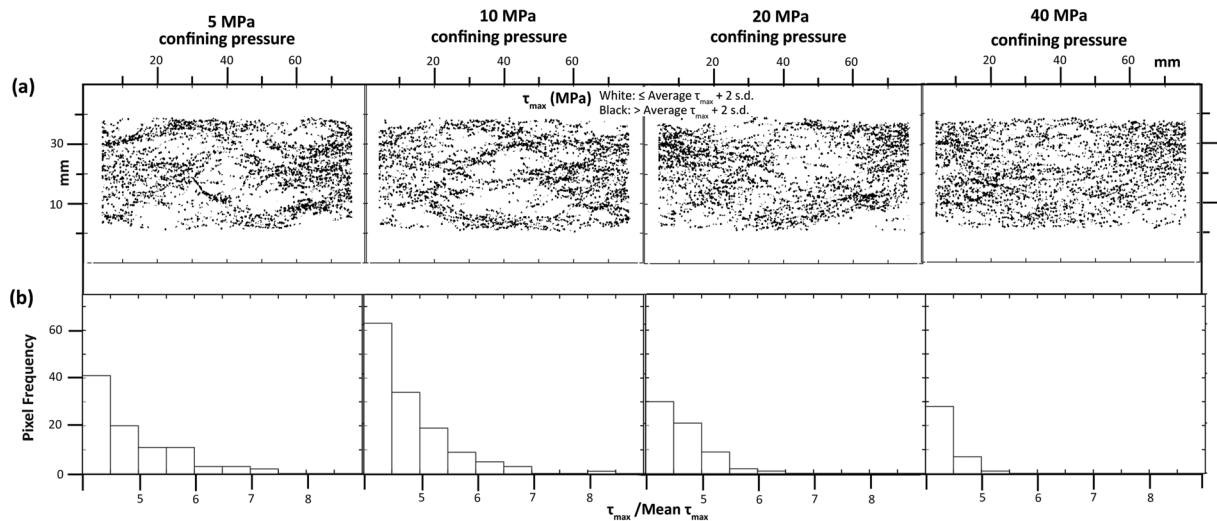


**Figure 9.** (a) Binary map highlighting spatial distribution of  $\tau_{\max}$  values greater than average plus two standard deviations for T2 series samples at postpeak configuration. (b) Corresponding histogram of the spatial distribution of  $\tau_{\max}$  in (a), normalized by the mean  $\tau_{\max}$ , showing decreasing heterogeneity with increasing confining pressure at postpeak configuration.

**Table 6**  
Roscoe Angle Data for Selected T2 Series Experiments

Test name	Roscoe Angle $\nu^\circ$ (assuming plane strain conditions)	Roscoe Angle $\nu^\circ$ (assuming triaxial conditions)	Shear band orientation with respect to $\sigma_3$ $\eta^\circ$ (average of left and right)
T2-05	6.1	6.3	62.5
T2-10	5.5	5.6	52
T2-20	−0.032	0.099	50
T2-40	−4.3	−4.3	45

This friction angle is low for a sandy sediment, but the low value can be attributed to enhanced particle rolling in our 2-D configuration. In natural 3-D systems, a wide range and abundance of particles increase the degree of interlocking resulting in greater friction (Hazzard & Mair, 2003; Morgan, 2004). Regardless of the actual value of friction, the variation in the friction angle as a function of confining pressure (equation (5)) is not consistent with the single value of friction angle irrespective of confining pressure obtained from the Mohr-Coulomb relationship (equation (6)). Therefore, we note that the Mohr-Coulomb failure criterion represents an average behavior of the sample over the range of confining pressures tested but is based only on stresses (e.g., Jaeger et al., 2007); it does not account for the role of volume changes and other related rock property changes during the failure process. We suggest that the systematic variation in the apparent friction angle results from changes in sample dilatancy, more consistent with predictions for granular materials and theoretical soil mechanics (Muir Wood, 1990). These volume changes are clearly demonstrated by our experiments where compaction occurs within the sample matrix while dilation occurs at the position of the fracture (Figures 8b and 8c). Additionally, the magnitude of dilation at the position of the fracture decreases with increasing confining pressure (Figure 8c). At lower confining pressures, a bulk dilation of the sample could result in more bond breakage in tension. When bonds break in tension, particles can separate from each other and move into the lower energy configurations, thus decreasing the fracture angle. At relatively higher confining pressures, in which a bulk compaction occurs, bond breakage in tension is hindered. Rather, bonds are preferentially broken in shear as particles slide past each other due to the high confinement.

The interplay between stress and porosity during deformation is illuminated in our experiments by the occurrence of high-magnitude stress chains across a fracture in our numerical experiments (Figure 11). The spatial distribution of stress at the position of the fracture is heterogeneous; it is generally less than the average spatial  $\tau_{\max}$  except in regions where high-magnitude stress chains occur across the fracture (Figure 11). These stress chains correspond to localized regions of low porosity where particles are concentrated, resulting in more contact area. With increasing confining pressure, the number of distinct, high-magnitude stress chains

across the through-going fracture decreases, whereas the number of particles that define the thickness of these stress chains increases (Figure 11 and Table 3). Thus, at relatively high confining pressures, local zones of compaction correspond to the occurrence of thick high-magnitude stress chains, that is,  $\sim 12$  particles wide, while local zones of dilation lack high-magnitude stress chains.

From our work, we show correlations between stress and porosity on the bulk scale and demonstrate our ability to analyze those correlations on the grain scale (Figures 2 and 3). Deformation is initially homogeneous, then becomes heterogeneous as indicated by the spatial variability of stress and porosity. The spatial variation of stress and porosity are related and show a dependence on confining pressure, which leaves an indelible mark on the rock that reflects its deformation history (e.g., varying depths of burial in a basin). Our results indicate that dilation is occurring at a scale that would be difficult to observe in natural samples (Figure 3), and different stress conditions create different microstructures within a shear band (Figure 11). This opens up the potential that the results of this work can be applied in a forensic sense to understand the stress conditions of brittle failure for samples

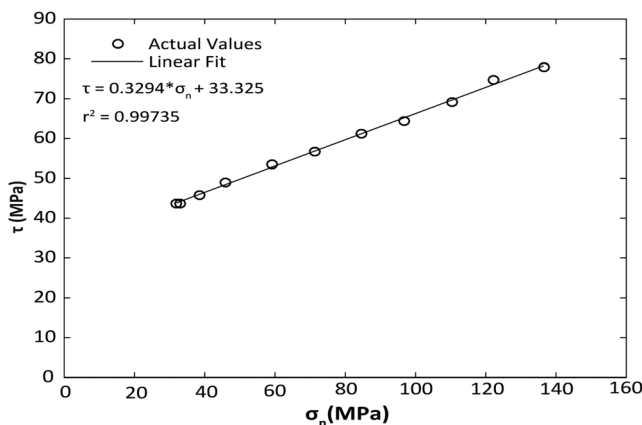


**Figure 10.** Mohr-Coulomb failure line derived from suite of biaxial experiments conducted on T2 series numerical samples. Identical particle assemblages are preconsolidated to 10 MPa and deformed under different confining pressures (Table 5).

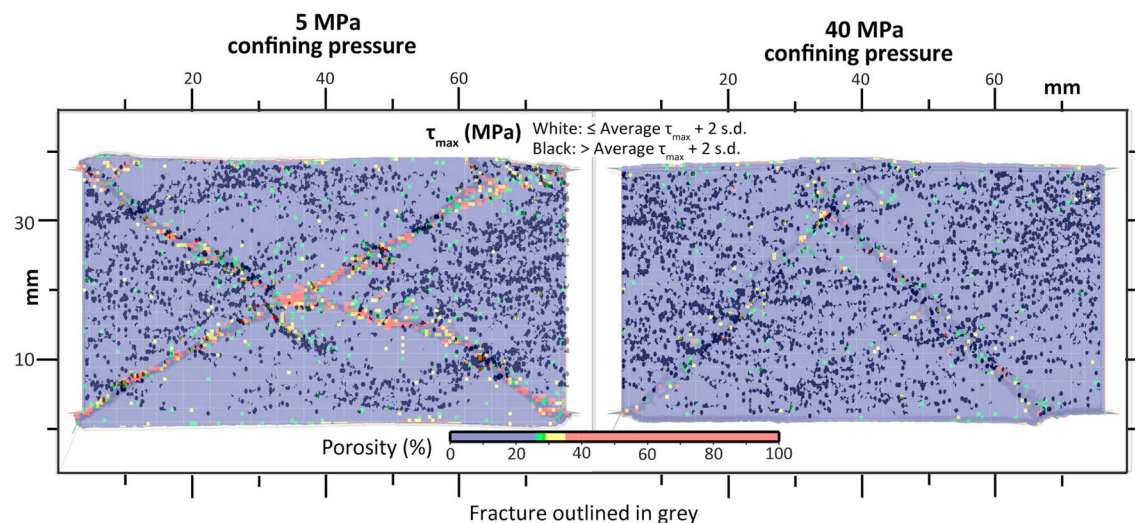


**Figure 11.** Overlay of binary map of  $\tau_{\max}$  with porosity at postpeak for Samples T2-05 and T2-40; fracture outlined in grey. High-magnitude stress chains occur across a fracture where porosity is low. The number of distinct chains across a fracture decreases, while the number of particles that define the thickness of the chains increases with increasing confining pressure.

obtained from the field. So depending on the degree of heterogeneity observed within the shear zone, it may be possible to infer a low or high confining pressure at the time of shear band formation. Additionally, our results will be useful to predict the locations of greatest increase and decrease in porosity at different depths in the Earth during brittle failure and can provide useful input for reservoir modeling. Because an increase in porosity can promote fluid flow, there is a need to understand how it is affected by increasing stresses with depth for the optimal location of water, hydrocarbon, and geothermal wells.

## 6. Conclusions

We present new perspectives on the evolution of stress, strain, and porosity of numerical analogs to low cohesive sandy sediment. We do this with DEM experiments that reproduce macroscopic behavior and deformation features, but also allow inspection of the micromechanical processes responsible for the macroscopic behavior. From our series of experiments that spanned confining pressures from 5 to 40 MPa, we conclude the following:

1. Fracturing is a progressive process that is accompanied by changes in  $\tau_{\max}$ , volumetric strain, distortional strain, and porosity from relatively uniform prior to peak stress to relatively localized postpeak stress.
2. Prior to peak stress, deformation occurs by the formation of localized bands of dilation, which eventually coalesce into through-going shear fractures.
3. Dilation is inhibited while distortional strain is promoted with increasing confining pressure.
4. Postpeak stress, shear fractures correspond to zones of higher porosity and generally lower stresses, but with local highs, and concentrated distortional strain.
  - a High stresses are transmitted across fractures where the porosity is lower, that is, through a network of particles in contact.
  - b The abundance of stress chains that span the sample is limited by the areas of contact along the fractures.
5. The number of distinct stress chains across a shear fracture decreases, while the thickness increases with increasing confining pressure.
6. Shear fractures steepen with increasing confining pressure.

## Acknowledgments

This work has been funded by the Department of Earth Science, Rice University. Computing facilities were made available through the Center for Computational Geophysics. The authors benefitted from discussions on geomechanics within our research group, and suggestions in data processing from John Cornthwaite. Modeling results and information can be obtained in supporting information or by contacting T. LongJohn at tami.longjohn94@gmail.com.

## References

- Alikarami, R., Andò, E., Gkiousas-Kapnis, M., Torabi, A., & Viggiani, G. (2014). Strain localisation and grain breakage in sand under shearing at high mean stress: Insights from in situ X-ray tomography. *Acta Geotechnica*, 10(1), 15–30. <https://doi.org/10.1007/s11440-014-0364-6>
- Alshibli, K. A., & Hasan, A. (2008). Spatial variation of void ratio and shear band thickness in sand using X-ray computed tomography. *Géotechnique*, 58(4), 249–257. <https://doi.org/10.1680/geot.2008.58.4.249>



- Al-Tahini, A. M., Sondergeld, C. H., & Rai, C. S. (2006). The effect of cementation on the mechanical properties of sandstones. *SPE Reservoir Evaluation & Engineering*, 9(04), 308–316. <https://doi.org/10.2118/89069-PA>
- Antonellini, M. A., & Pollard, D. D. (1995). Distinct element modelling of deformation bands in sandstone. *Journal of Structural Geology*, 17(8), 1165–1182. [https://doi.org/10.1016/0191-8141\(95\)00001-T](https://doi.org/10.1016/0191-8141(95)00001-T)
- Berkowitz, B. (2002). Characterizing flow and transport in fractured geological media: A review. *Advances in Water Resources*, 25(8–12), 861–884. [https://doi.org/10.1016/S0309-1708\(02\)00042-8](https://doi.org/10.1016/S0309-1708(02)00042-8)
- Bernab , Y., Mok, U., & Evans, B. (2003). Permeability-porosity relationships in rocks subjected to various evolution processes. *Pure and Applied Geophysics*, 160(5), 937–960. <https://doi.org/10.1007/PL00012574>
- B suelle, P., Desrues, J., & Raynaud, S. (2000). Experimental characterisation of the localisation phenomenon inside a Vosges sandstone in a triaxial cell. *International Journal of Rock Mechanics and Mining Sciences*, 37(8), 1223–1237. [https://doi.org/10.1016/S1365-1609\(00\)00057-5](https://doi.org/10.1016/S1365-1609(00)00057-5)
- Bieniawski, Z. T. (1967a). Mechanism of brittle fracture of rock: Part I—Theory of the fracture process. *International Journal of Rock Mechanics and Mining Sciences*, 4(4), 395–406. [https://doi.org/10.1016/0148-9062\(67\)90030-7](https://doi.org/10.1016/0148-9062(67)90030-7)
- Bieniawski, Z. T. (1967b). Mechanism of brittle fracture of rock. Part II—Experimental Studies. *International Journal of Rock Mechanics and Mining Sciences*, 4(4), 407–423. [https://doi.org/10.1016/0148-9062\(67\)90031-9](https://doi.org/10.1016/0148-9062(67)90031-9)
- Boutt, D. F., & McPherson, B. J. O. L. (2002). Simulation of sedimentary rock deformation: Lab-scale model calibration and parameterization. *Geophysical Research Letters*, 29(4), 1054. <https://doi.org/10.1029/2001GL013987>
- Brace, W. F., & Byerlee, J. D. (1966). Recent experimental studies of brittle fracture of rocks. *American Rock Mechanics Association*, 92, 10–12. <https://doi.org/10.1111/j.1600-0404.1995.tb01704.x>
- Brace, W. F., Paulding, B. W., & Scholz, C. (1966). Dilatancy in the fracture of crystalline rocks. *Journal of Geophysical Research*, 71(16), 3939–3953. <https://doi.org/10.1029/JZ071i016p03939>
- Chang, C., Zoback, M. D., & Khaksar, A. (2006). Empirical relations between rock strength and physical properties in sedimentary rocks. *Journal of Petroleum Science and Engineering*, 51(3–4), 223–237. <https://doi.org/10.1016/j.petrol.2006.01.003>
- Coates, D. F. (1964). Classification of rocks for rock mechanics. *International Journal of Rock Mechanics and Mining Sciences*, 1(3), 421–429. [https://doi.org/10.1016/0148-9062\(64\)90008-7](https://doi.org/10.1016/0148-9062(64)90008-7)
- Cundall, P. A., & Strack, O. D. L. (1979). A discrete numerical model for granular assemblies. *G otechnique*, 29(1), 47–65. <https://doi.org/10.1680/geot.1979.29.1.47>
- Dean, S. L., Morgan, J. K., & Fournier, T. (2013). Geometries of frontal fold and thrust belts: Insights from discrete element simulations. *Journal of Structural Geology*, 53, 43–53. <https://doi.org/10.1016/j.jsg.2013.05.008>
- Desrues, J., Lanier, J., & Stutz, P. (1985). Localization of the deformation in tests on sand sample. *Engineering Fracture Mechanics*, 21(4), 909–921. [https://doi.org/10.1016/0013-7944\(85\)90097-9](https://doi.org/10.1016/0013-7944(85)90097-9)
- Ding, X., Zhang, L., Zhu, H., & Zhang, Q. (2014). Effect of model scale and particle size distribution on PFC3D simulation results. *Rock Mechanics and Rock Engineering*, 47(6), 2139–2156. <https://doi.org/10.1007/s00603-013-0533-1>
- Driskill, B., Walls, J., DeVito, J., & Sinclair, S. W. (2013). Applications of SEM imaging to reservoir characterization in the Eagle Ford Shale, South Texas, U.S.A. *Electron Microscopy of Shale Hydrocarbon Reservoirs: AAPG Memoir*, 102, 115–136. <https://doi.org/10.1306/13391709M1023587>
- El Bied, A., Sulem, J., & Martineau, F. (2002). Microstructure of shear zones in Fontainebleau sandstone. *International Journal of Rock Mechanics and Mining Sciences*, 39(7), 917–932. [https://doi.org/10.1016/S1365-1609\(02\)00068-0](https://doi.org/10.1016/S1365-1609(02)00068-0)
- Feng, X. T., Chen, S., & Zhou, H. (2004). Real-time computerized tomography (CT) experiments on sandstone damage evolution during triaxial compression with chemical corrosion. *International Journal of Rock Mechanics and Mining Sciences*, 41(2), 181–192. [https://doi.org/10.1016/S1365-1609\(03\)00059-5](https://doi.org/10.1016/S1365-1609(03)00059-5)
- Fossen, H., Schultz, R. A., Shipton, Z. K., & Mair, K. (2007). Deformation bands in sandstone: a review. *Journal of the Geological Society*, 164, 1–15. <https://doi.org/10.1144/0016-76492006-036>
- Friedman, M. (1976). Porosity, permeability, and rock mechanics—A review, 15(February).
- Guo, Y., & Morgan, J. K. (2004). Influence of normal stress and grain shape on granular friction: Results of discrete element simulations. *Journal of Geophysical Research*, 109, B12305. <https://doi.org/10.1029/2004JB003044>
- Guo, Y., & Morgan, J. K. (2007). Fault gouge evolution and its dependence on normal stress and rock strength—Results of discrete element simulations: Gouge zone properties. *Journal of Geophysical Research*, 112, B10403. <https://doi.org/10.1029/2006JB004524>
- Guo, Y., & Morgan, J. K. (2008). Fault gouge evolution and its dependence on normal stress and rock strength—Results of discrete element simulations: Gouge zone micromechanics. *Journal of Geophysical Research*, 113, B08417. <https://doi.org/10.1029/2006JB004525>
- Hallbauer, D. K., Wagner, H., & Cook, N. G. W. (1973). Some observations concerning the microscopic and mechanical behaviour of quartzite specimens in stiff, triaxial compression tests. *International Journal of Rock Mechanics and Mining Sciences*, 10(6), 713–726. [https://doi.org/10.1016/0148-9062\(73\)90015-6](https://doi.org/10.1016/0148-9062(73)90015-6)
- Handin, J., & Hager, R. V. (1957). Experimental deformation of sedimentary rocks under confining pressure: Tests at room temperature on dry samples. *Bulletin of the American Association of Petroleum Geologists*, 41(1).
- Handin, J., Hager, R. V., Friedman, M., & Feathers, J. N. (1963). Experimental deformation of sedimentary rocks under confining pressure: Pore pressure tests. *Bulletin of the American Association of Petroleum Geologists*, 51(1323), 468–470. <https://doi.org/10.1126/science.51.1323.468>
- Hazzard, J. F., & Mair, K. (2003). The importance of the third dimension in granular shear. *Geophysical Research Letters*, 30(13), 1708. <https://doi.org/10.1029/2003GL017534>
- Hirata, A., Kameoka, Y., & Hirano, T. (2007). Safety management based on detection of possible rock bursts by AE monitoring during tunnel excavation. *Rock Mechanics and Rock Engineering*, 40(6), 563–576. <https://doi.org/10.1007/s00603-006-0122-7>
- Hoek, E., & Martin, C. D. (2014). Fracture initiation and propagation in intact rock - a review. *Journal of Rock Mechanics and Geotechnical Engineering*, 6(4), 287–300. <https://doi.org/10.1016/j.jrmge.2014.06.001>
- Howell, D., Behringer, R., & Veje, C. (1999). Stress fluctuations in a 2D granular Couette experiment: A continuous transition. *Physical Review Letters*, 82(26), 5241–5244. <https://doi.org/10.1103/PhysRevLett.82.5241>
- Jaeger, J. C., Cook, N. G., & Zimmerman, R. W. (2007). *Fundamentals of Rock Mechanics* (4th ed.). Malden: Blackwell Publishing.
- Jiang, M., Yan, H. B., Zhu, H. H., & Utili, S. (2011). Modeling shear behavior and strain localization in cemented sands by two-dimensional distinct element method analyses. *Computers and Geotechnics*, 38(1), 14–29. <https://doi.org/10.1016/j.compgeo.2010.09.001>
- Jiang, M., Liu, J., Sun, Y., & Yin, Z. (2013). Investigation into macroscopic and microscopic behaviors of bonded sands using distinct element method. *Soils and Foundations*, 53(6), 804–819. <https://doi.org/10.1016/j.sandf.2013.10.001>
- Jiang, M., Zhang, W., Sun, Y., & Utili, S. (2013). An investigation on loose cemented granular materials via DEM analyses. *Granular Matter*, 15(1), 65–84. <https://doi.org/10.1007/s10035-012-0382-8>

- Jiang, M., Zhang, F., & Thornton, C. (2015). A simple three-dimensional distinct element modeling of the mechanical behavior of bonded sands. *International Journal for Numerical and Analytical Methods in Geomechanics*, 39(16), 1791–1820.
- Katz, O., Morgan, J. K., Aharonov, E., & Dugan, B. (2014). Controls on the size and geometry of landslides: Insights from discrete element numerical simulations. *Geomorphology*, 220, 104–113.
- Kock, I., & Huhn, K. (2007a). Influence of particle shape on the frictional strength of sediments—A numerical case study. *Sedimentary Geology*, 196(1–4), 217–233. <https://doi.org/10.1016/j.sedgeo.2006.07.011>
- Kock, I., & Huhn, K. (2007b). Numerical investigation of localization and micromechanics in a stratified soil specimen. *Journal of Structural Geology*, 29(10), 1679–1694. <https://doi.org/10.1016/j.jsg.2007.07.013>
- Lambe, T. W., & Whitman, R. V. (Eds.) (1969). *Soil Mechanics*. New York: John Wiley & Sons, Inc.
- Ma, C., & Chen, G. (2016). Microseismic characterization of brittle fracture mechanism in highly stressed surrounding rock mass, 1–5.
- Maltman, A. J., Jones, M. E., Murray, T., Collinson, J. D., Martinsen, O. J., Karig, D. E., et al. (1994). In A. J. Maltman (Ed.), *The Geological Deformation of Sediments* (1st ed.). London: Chapman and Hall.
- Menendez, B., Zhu, W., & Wong, T. F. (1996). Micromechanics of brittle faulting and Cataclastic flow in Berea sandstone. *Science*, 18(1).
- Morgan, J. K. (2004). Particle dynamics simulations of rate- and state-dependent frictional sliding of granular fault gouge. *Pure and Applied Geophysics*, 161(9–10), 1877–1891. <https://doi.org/10.1007/s00024-004-2537-y>
- Morgan, J. K. (2015). Effects of cohesion on the structural and mechanical evolution of fold and thrust belts and contractional wedges: Discrete element simulations. *Journal of Geophysical Research*, 120, 1–27. <https://doi.org/10.1002/2014JB011455>
- Muir Wood, D. (1990). Soil Behaviour and Critical State Soil Mechanics. *Soil behaviour and critical state soil mechanics*, 29(4), 211–212. [https://doi.org/10.1016/0148-9062\(92\)90570-P](https://doi.org/10.1016/0148-9062(92)90570-P)
- Nelson, R. A. (2001). *Geologic Analysis of Naturally Fractured Reservoirs* (2nd ed.). Woburn: Butterworth-Heinemann.
- Oda, M., & Iwashita, K. (1990). *Mechanics of Granular Materials: An Introduction*. Rotterdam: A.A.Balkema.
- Paterson, M. S., & Wong, T. F. (2005). *Experimental rock deformation-the brittle field*. New York: Springer Science & Business Media.
- Peters, J. F., Muthuswamy, M., Wibowo, J., & Tordesillas, A. (2005). Characterization of force chains in granular material. *Physical Review E - Statistical, Nonlinear, and Soft Matter Physics*, 72(4), 1–8. <https://doi.org/10.1103/PhysRevE.72.041307>
- Salvatore, E., Andò, E., Viggiani, G., & Modoni, G. (2016). Compression and extension triaxial tests on sand, studied with X-ray microtomography and digital image correlation. *1st IMEKO TC-4 International Workshop on Metrology for Geotechnics*, 157–161.
- Schock, R. N., Heard, H. C., & Stephens, D. R. (1973). Stress-strain behavior of a granodiorite and two graywackes on compression to 20 kilobars. *Journal of Geophysical Research*, 78(26), 5922–5941. <https://doi.org/10.1029/JB078i026p05922>
- Schöpfer, M. P. J., Abe, S., Childs, C., & Walsh, J. J. (2009). The impact of porosity and crack density on the elasticity, strength and friction of cohesive granular materials: Insights from DEM modelling. *International Journal of Rock Mechanics and Mining Sciences*, 46(2), 250–261. <https://doi.org/10.1016/j.ijrmms.2008.03.009>
- Stearns, D. W., & Friedman, M. (1972). Reservoirs in fractured rock. *Stratigraphic Oil and Gas Fields- Classification, Exploration Methods, and Case Histories*, M16, 82–100.
- Sulem, J., & Ouffroukh, H. (2006). Shear banding in drained and undrained triaxial tests on a saturated sandstone: Porosity and permeability evolution. *International Journal of Rock Mechanics and Mining Sciences*, 43(2), 292–310. <https://doi.org/10.1016/j.ijrmms.2005.07.001>
- Wessel, P., & Smith, W. H. F. (1995). The Generic Mapping Tools (GMT) Version 3.0. *Technical Reference & Cookbook*, Sch. of Ocean and Earth Sci. and Technol, Honolulu, Hawaii.
- Wong, T.-F., David, C., & Zhu, W. (1997). The transition from brittle faulting to cataclastic flow in porous sandstones: Mechanical deformation. *Journal of Geophysical Research*, 102(B2), 3027–3041. <https://doi.org/10.1029/96JB03282>
- Zuriguel, I., & Mullin, T. (2008). The role of particle shape on the stress distribution in a sandpile. *Proceedings of the Royal Society A: Mathematical, Physical and Engineering Science*, 464(2089), 99–116. <https://doi.org/10.1098/rspa.2007.1899>